Ionics (2019) 25:685–695
https://doi.org/10.1007/s11581-018-2680-6

ORIGINAL PAPER

Facile one-step hydrothermal synthesis of PEDOT:PSS/MnO_2 nanorod hybrids for high-rate supercapacitor electrode materials

Chengjie Yin[1] · Hongming Zhou[1,2] · Jian Li[1,2]

Received: 14 June 2018 / Revised: 30 July 2018 / Accepted: 2 August 2018 / Published online: 14 August 2018

Abstract

Poly(3,4-ethylenedioxythiophene)–polystyrenesulfonate and manganese oxide (PEDOT:PSS/MnO_2) hybrids were prepared via a facile solvothermal method coupled with an oxidative polymerization route. The effects of the reaction temperature and the $KMnO_4$-to-organic monomer (3,4-ethylenedioxythiophene, EDOT) ratio on the morphology, structure, and electrochemical properties of the materials were investigated. The optimized composites comprised homogeneous nanorod-like structures and exhibited overwhelmingly high conductivity (36 S cm^{-1}) and superior supercapacitance—more specifically, they exhibited high-rate capability. The electrochemical properties of the nanocomposites were investigated using cyclic voltammetry and galvanostatic charge–discharge cycling. The prepared hybrids showed a high capacitance of 365.5 F g^{-1} at a current density of 1 A g^{-1}, a good rate performance of 325.4 F g^{-1} at 20 A g^{-1} (capacitance retention of 89%), and excellent cycling stability with approximately 80% capacitance retention after 2000 cycles at a current density of 5 A g^{-1} in a 6 M KOH aqueous electrolyte.

Keywords Manganese dioxide · PEDOT:PSS · High-rate performance · Synthesis · Supercapacitor

Introduction

Recently, high-energy and high-power-density storage devices have attracted considerable research interest due to their increasing demand for certain vehicle applications [1–4]. Supercapacitors, also known as electrochemical capacitors, are divided into pseudocapacitors (fast surface redox reactions) and electrochemical double-layer capacitors (ion adsorption) [5–7] on the basis of their energy storage mechanism. The electrochemical performance of supercapacitors depends on their electrode materials; therefore, the synthesis and modification of electrode materials for supercapacitors has become an active research topic. Compared with double-layer capacitors, pseudocapacitors exhibit superior electrochemical performance because of their redox mechanism [8, 9]. In most cases, the electroactive materials for high-performance pseudocapacitor electrodes predominantly comprise a transition-metal oxide (e.g., MnO_2 [10], Fe_3O_4 [11], Co_3O_4 [12], NiO [13], or $NiCo_2O_4$ [14]), a conducting polymer (e.g., polypyrrole [15], polyaniline [16], or poly(3,4-ethylenedioxythiophene) (PEDOT) [17]), or one of their derivatives [18, 19].

Among the aforementioned materials, MnO_2 is one of the most promising electrode materials and offers numerous advantages. For instance, it exhibits a high theoretical specific capacitance (1370 F g^{-1}) and is naturally abundant and environmentally friendly [20, 21]. It has therefore been the subject of intensive investigation. However, MnO_2 has an intrinsically limited conductivity (10^{-5} to 10^{-6} S cm^{-1}), which hinders its application to high-performance supercapacitors [22, 23]. To solve this problem, researchers have developed several strategies such as depositing MnO_2 onto highly conductive materials such as carbon nanotubes [24–26], graphene [27–29], or metal oxide tubes [30–32]. However, only a few studies have involved depositing MnO_2 onto a conducting polymer. In this study, a conducting polymer such as PEDOT doped with polystyrenesulfonate (PSS), which exhibits high flexibility and high conductivity of approximately 10^3 S cm^{-1} [33–35], is complexed with MnO_2; this complexation improves the

Electronic supplementary material The online version of this article (https://doi.org/10.1007/s11581-018-2680-6) contains supplementary material, which is available to authorized users.

✉ Hongming Zhou
zhouhongming@csu.edu.cn

✉ Jian Li
ziliao2000@126.com

[1] School of Materials Science and Engineering, Central South University, Changsha 410083, Hunan, China

[2] Hunan Zhengyuan Institute for Energy Storage Materials and Devices, Changsha 410083, Hunan, China

conductivity of the resultant composite and also provides buffering against the structural collapse of MnO_2 resulting from volume expansion during the charge–discharge process.

PEDOT/MnO_2 is prepared via a two-step method. In general, the first step is the synthesis of PEDOT, followed by the deposition of MnO_2 onto the polymer surface via an in situ deposition method. Various precursors have been used to prepare MnO_2, and various methods have been investigated for combining MnO_2 with PEDOT through electrochemical deposition, in situ polymerization, etc. Several researchers have also reported the synthesis and characterization of PEDOT/MnO_2 hybrids. For instance, Tang and Han prepared graphite/PEDOT/MnO_2 hybrids with controlled network structures on commercial separator membranes via chemical oxidation polymerization and electrochemical deposition; the resultant electrodes exhibited a specific capacitance of 195.7 F g^{-1} at a current density of 0.5 A g^{-1} and retained 81.1% of their capacity after 2000 cycles [36]. Su et al. prepared MnO_2/PEDOT:PSS electrodes through a simple co-electrodeposition process; the electrodes demonstrated a high areal capacitance of 1670 mF cm^{-2} at 0.5 mA cm^{-2} [37]. Yu et al. designed and fabricated an Ag/PEDOT:PSS/MnO_2 layer-by-layer structure with excellent specific capacitance (862 F g^{-1} at 2.5 A g^{-1}) [38]. However, the preparation of PEDOT/MnO_2 hybrids via a one-step route has rarely been reported. Lee et al. used one-step co-electrodeposition to prepare MnO_2/PEDOT coaxial nanowires with a good electrochemical performance of 210 F g^{-1} at 1 mA cm^{-2} [39–42].

Herein, we report a facile one-step hydrothermal oxidative polymerization method to prepare PEDOT:PSS/MnO_2 hybrids to be used as high-rate supercapacitor electrode materials. Specifically, a PEDOT:PSS/MnO_2 hybrid nanocomposite is obtained via a one-step method in which $KMnO_4$ is used as the oxidant and the manganese source and 3,4-ethoxylenedioxythiophene (EDOT) are used as the reducing agents. In this study, the reaction temperature and the $KMnO_4$-to-EDOT molar ratio were optimized; the formation mechanism of the PEDOT:PSS/MnO_2 nanorods was also discussed. The optimized PEDOT:PSS/MnO_2 nanorods exhibited a high conductivity (36 S cm^{-1}), a high specific capacitance of 365.5 F g^{-1} at 1 A g^{-1}, and a good rate performance of 325.4 F g^{-1} at 20 A g^{-1} (capacitance retention of 89%). The preparation route proposed here offers a new direction for the synthesis of organic polymer/metal oxide composites.

Materials and methods

Chemical reagents and materials

All the reagents used in this study were of analytical grade and were used without further purification. Ethanol was purchased from Tianjin Fengchuan Chemical Reagent Co., Ltd. $KMnO_4$ was obtained from Hengyang Kaixin Chemical Reagent Co., Ltd. EDOT and PSS (MW = 80,000, mass fraction = 25%) was provided by Maklin. The nickel foam (1 × 4 cm^2, Sigma-Aldrich) was cleaned by sequential sonication in 3 M HCl, acetone, distilled water, and absolute ethanol for 15 min.

Synthesis of PEDOT:PSS/MnO_2 Nanorods

A schematic of the synthesis procedures for the PEDOT:PSS/MnO_2 hybrids is shown in Fig. 1. The PEDOT:PSS/MnO_2 nanorod hybrid was prepared by a one-pot solvothermal oxidative polymerization route. According to the typical procedure, 7.6 g of PSS (the molar ratio of $-SO_3^-$ in PSS:EDOT = 1.5:1) was dispersed in 40 mL of alcohol solution ($V_{ethanol}$:V_{water} = 1:1). Then, 0.9 g of EDOT was added and the mixture was stirred under sonication for 10 min, resulting in the formation of a homogeneous emulsion. After 50 mL of $KMnO_4$ aqueous solution ($KMnO_4$-to-EDOT molar ratios of 3:6, 4:6, 5:6, and 6:6) was added to the obtained emulsion with sonication for 10 min, an ambiguous suspension was formed. The mixture was transferred to a 150-mL Teflon-lined autoclave and heated at 100 °C for 15 h. The black precipitates were collected and subsequently washed several times with distilled water and absolute ethanol. The PEDOT:PSS/MnO_2 was dried at 60 °C overnight under vacuum.

In separate experiments, the reaction temperature and the molar ratio of $KMnO_4$ were investigated with respect to their influence on the electrochemical properties of the resultant hybrid nanocomposites. PEDOT:PSS/MnO_2 hybrids with different $KMnO_4$-to-EDOT molar ratios (3:6, 4:6, 5:6, and 6:6, labeled as PPM3O, PPM4O, PPM5O, and PPM6O, respectively) and under different reaction temperatures (60 °C, 80 °C, 100 °C, and 120 °C, labeled as PPMO6, PPMO8, PPMO10, and PPMO12, respectively; $KMnO_4$:EDOT = 4:6) were prepared using a similar procedure.

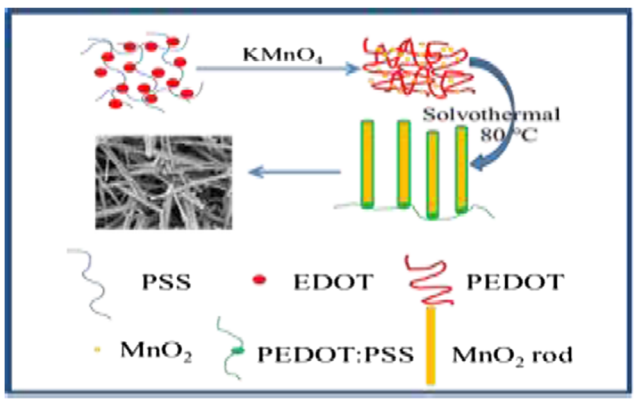

Fig. 1 Schematic illustration of the synthesis procedures for PEDOT:PSS/MnO_2 hybrid

Characterization

Fourier transform infrared (FT-IR) spectroscopy was performed using a Nexus 670 IR spectrometer to characterize the bonding parameters of the prepared samples. X-ray diffraction (XRD) was conducted on a Rigaku 2550 X-ray diffractometer equipped with a Cu Kα X-ray source to determine whether crystallites had formed. Field-emission scanning electron microscopy images were obtained on a Hitachi SU8010 at an acceleration voltage of 10 kV. Thermogravimetric analysis (TGA) was conducted on a Q500 thermogravimetric analyzer; samples were heated at 10 °C min^{-1} from 0 to 800 °C under nitrogen gas flowing at 100 mL min^{-1}. Conductivity measurements were obtained using an SDY-4 conductivity meter via four-probe conductivity measurements.

Working electrode fabrication and electrochemical measurements

The working electrodes were prepared using a slurry composed of 90% PEDOT:PSS/MnO_2 hybrids as the active material, 5% acetylene black, and 5% poly(tetrafluoroethylene). The prepared slurry was pasted onto pretreated foam nickel substrates. The mass loading of active material in the working electrode was approximately 1 mg cm^{-2}. The electrochemical measurements were performed in a three-electrode system with the prepared electrode as the working electrode, Pt as the counter electrode, Ag/AgCl as the reference electrode, and 6 M KOH aqueous solution as the electrolyte. Galvanostatic charge–discharge measurements were performed in the potential voltage from −0.1 to 0.6 V. Cyclic voltammetry (CV) was conducted on an RST 5200 electrochemical workstation in the stable potential range from −0.1 to 0.6 V. The specific capacitance of the resulting materials was calculated using the equation $Cs = (I \times \Delta t) / (\Delta V \times m)$, where m (g) is the mass of the active material, and Δt (s), I (A), and ΔV (V) are the discharge time, charge–discharge current, and potential window, respectively.

Results and discussion

Structures and morphologies

Information about the structure and chemical bonding of the PEDOT:PSS/MnO_2 hybrids was obtained via FT-IR; the infrared spectra are shown in Fig. 2, where the peaks of the characteristic group in the PEDOT polymer, the functional-group peaks of the PSS dopant, and the vibrational peaks of Mn–O in MnO_2 are observed. Figure 2a shows that the peak positions in the spectra of PEDOT:PSS/MnO_2 changed as the content of $KMnO_4$ was changed. Specifically, the absorption peak at approximately 1612 cm^{-1} is attributed to the stretching vibration of the O–H bonds of hydroxyl groups adsorbed onto the surface of metal atoms [43]; this peak shifted first to a lower wavenumber of 1608 cm^{-1} and then to a higher wavenumber of 1618 cm^{-1} with increasing $KMnO_4$-to-EDOT molar ratio. The vibration absorption peak at 1361 cm^{-1} is attributed to C–C bonds in the thiophene ring; the peaks at approximately 1151 and 1085 cm^{-1} correspond to the stretching vibration peak of the C–O–C moiety of the dioxyethylene ring. With increasing $KMnO_4$ content, these peaks gradually shifted to lower wavenumbers, indicating that the polymerization and conjugation degree of the PEDOT chains increased with increasing oxidant content. The peak at 858 cm^{-1}, which is assigned to the C–S vibration in the thiophene ring in conjunction with the aforementioned IR peaks of the other functional groups, confirms that the polymer PEDOT was successfully prepared. The absorption peaks at 593 cm^{-1} and 449 cm^{-1} in Fig. 2b are the stretching peaks of the Mn–O bonds in inorganic MnO_2, which can provide important evidence for the existence of MnO_2 in composites. With increasing $KMnO_4$ content, the Mn–O peak intensity also increased primarily because an increase in the amount of $KMnO_4$ led to an increase in the content of MnO_2 in the composites. In addition, the peak at 1037 cm^{-1} is the absorption vibrational peak of $–SO_3^-$ in PSS, indicating that the PEDOT was successfully doped with PSS [44]. As is evident in Fig. 2, with increasing reaction temperature, the peaks associated with organic matter decreased in intensity mainly because of the decomposition of hybrid PEDOT:PSS/MnO_2 during long-term exposure to high temperatures and high pressures. Therefore, controlling the oxidant ratio and reaction temperature was the key to preparing a superior composite.

The XRD patterns of composites prepared by hydrothermal reactions under different experimental conditions are given in Fig. 3. We investigated the effects of the $KMnO_4$-to-EDOT molar ratio and the reaction temperature on the nucleation, crystal growth, and crystal structure of the prepared materials. Characteristic diffraction peaks of MnO_2 were observed in the XRD patterns of PPM6O, PPMO10, and PPMO12. As shown in Fig. 3a, when the $KMnO_4$-to-EDOT molar ratio was 3:6, the MnO_2 peak was not obvious mainly because less MnO_2 and OH^- were generated during the oxidation process when the content of $KMnO_4$ was low; the mixture was consequently weakly alkaline, which is not conducive to the formation of crystalline MnO_2. Thus, the XRD pattern shows only a wide diffraction peak at 18.6°, which is assigned to the polymer molecular chain of PEDOT [44, 45]. When the concentration of the $KMnO_4$ oxidant was increased, the XRD pattern of the resultant PPM6O showed diffraction peaks of 28.6°, 37.5°, 41.5°, 55.3°, 60.2°, 65.7°, and 72.6°, corresponding to the (110), (101), (111), (211), (220), (200), and (301) crystal planes of β-MnO_2 (JCPDS No. 24-0735). The overall variation was that the degree of crystallinity of the composites

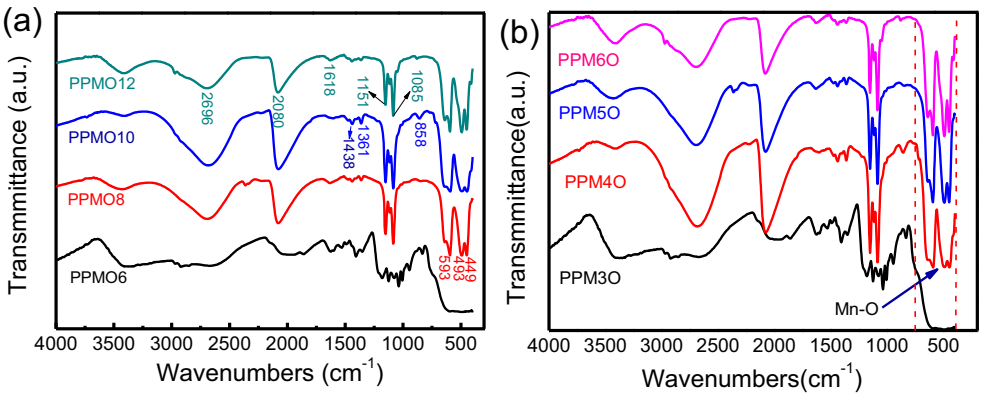

Fig. 2 FI–IR spectra of prepared materials, **a** materials prepared at hydrothermal temperature of 60 °C, 80 °C, 100 °C and 120 °C, respectively; **b** materials prepared at the $n(KMnO_4)$: n (EDOT) = 3/6, 4/6, 5/6 and 6/6, respectively

changed from amorphous to crystalline and the diffraction peaks of MnO_2 increased in intensity with increasing $KMnO_4$ content. This behavior is mainly attributed to the following equilibrium: [46]

$$3n\ \mathrm{EDOT} + 2n\ \mathrm{MnO_4^-} \rightleftharpoons 3\ \mathrm{P(EDOT)}n + 2n\ \mathrm{MnO_2} + \mathrm{OH^-}$$

According to this equation, the content of MnO_2 in the composite mainly depends on the oxidant content. It shows that the ratio of $KMnO_4$ not only affects the oxidation degree of the organic EDOT but also profoundly influences the crystallization of MnO_2. Figure 3b shows that with increasing hydrothermal reaction temperature, the diffraction peaks of the materials also increased in intensity and became increasingly sharp; conversely, at higher temperatures, amorphous MnO_2 transformed into β-MnO_2, which became increasingly crystalline. This process is principally attributed to the increase in the contact probability between the $KMnO_4$ oxidant and the EDOT organic monomer with increasing temperature, which leads to higher pressures in the reactor and accelerates the formation rate of MnO_2. Simultaneously, the degree of supersaturation of MnO_2 was reduced, which reduced the nucleation rate. Generally, higher temperatures resulted in slower formation rates of new crystal nuclei of MnO_2; thus, the nucleation of the grains was no longer spontaneous, which limited the growth of MnO_2 on nucleated crystals, thereby improving crystallinity. In the subsequent analysis of the electrochemical performance of the composites, PPM4O delivered the best performance. The XRD curve of PPM4O, however, displays few visible diffraction peaks corresponding to MnO_2, revealing that MnO_2 in the PEDOT:PSS/MnO_2 hybrid was amorphous.

Figure 4 shows SEM images of materials prepared under different hydrothermal temperatures and different $KMnO_4$-to-EDOT molar ratios; these experiments were designed to explore the influence of reaction conditions on the morphology of the composites. The electron micrographs show a 1-μm size selection. Figure 4a, b, c, d shows that the morphology of the materials obtained at the various hydrothermal reaction temperatures was mainly substantial aggregation blocks and a spot of nanorods. The images of PPMO8 show nanorods with a length of 1 μm and a diameter of approximately 100 nm, the conclusion can also be proved in Fig. 5c, d. The micrographs of materials prepared at higher temperatures show that the nanorods were partially decomposed and collapsed at 100 and 120 °C and that the micrometer rods became irregular. These results demonstrate that the hydrothermal reaction temperature plays a decisive role in determining the morphology of the material. Temperatures lower than 60 °C were insufficient to favor the formation of MnO_2 crystals with rod-like morphology; more crystals existed in the form of aggregated

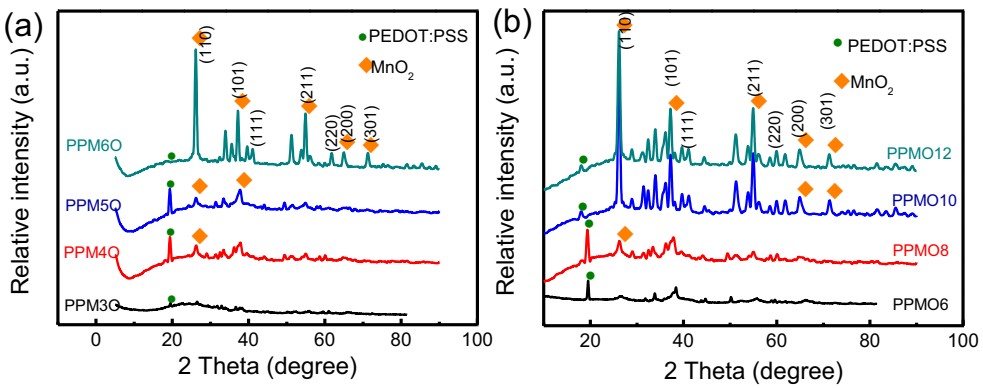

Fig. 3 XRD patterns of PEDOT:PSS/MnO_2 under different preparation conditions, **a** $n(KMnO_4)$ to n(EDOT) (3:6, 4:6, 5:6, and 6:6), **b** different hydrothermal temperature, respectively, 60 °C, 80 °C, 100 °C, and 120 °C

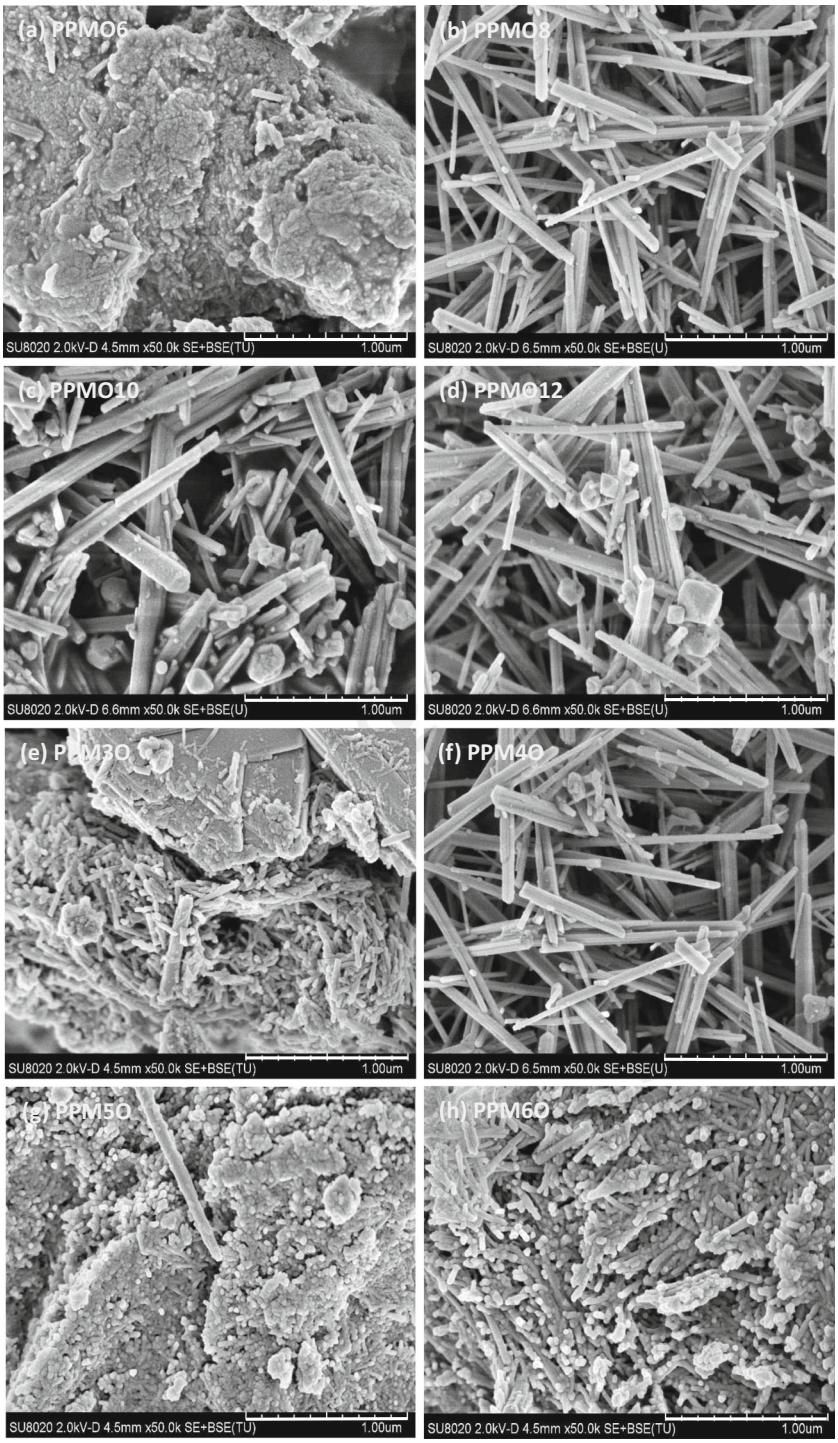

Fig. 4 SEM images of materials prepared under different hydrothermal temperature and ratio of $KMnO_4$ to EDOT

nanoparticles. In contrast, the morphology of the PEDOT:PSS organic polymers was banded or blocky under the experimental conditions and did not cause the collapse and decomposition of organic matter; thus, bulk aggregates with nanorod morphology were observed. When the temperature was increased to 80 °C, the temperature was conducive for the formation of MnO_2 microrods, whereas the organic molecular chains decomposed; this material could be well dispersed because the decomposition of organic matter reduced the organic content, mainly resulting in MnO_2 micron-sized rods. Consequently, uniform-sized rod-like PEDOT:PSS/MnO_2 hybrids were obtained. When the temperature was increased further, some of the microrods were damaged. Microrods were decomposed into numerous nanoblocks; therefore, the morphology of the materials obtained at 100 and 120 °C comprised micrometer rods and nanoblocks with different sizes.

The nucleation mechanism of MnO_2 was predicted on the basis of the electron microscopy results. Under hydrothermal conditions, first, a large number of MnO_2 nuclei are rapidly produced during $KMnO_4$ oxidation of the organic monomers; the crystal nuclei grow in the same direction and assemble themselves into small solid spheres. Since the K^+ ions in the solution serve as a supporting lattice, the dopant PSS in the solution functions as a heterogeneous particle in the secondary crystallization of the crystal and affects the growth direction of MnO_2 crystals; thus, crystals grow along rod-like structures. At lower temperatures, insufficient energy is present for the formation of MnO_2 crystals. The crystal nuclei are only short sticks interwoven with blocks; thus, no anisotropic growth occurs.

Figure 4e, f, g, h depicts the SEM micrographs of the composites prepared at $KMnO_4$-to-EDOT molar ratios of 3:6, 4:6, 5:6, and 6:6, respectively. The graph shows that when the molar ratio was 3:6, nanorods and blocks coexisted in the material; as the molar ratio was increased, the nanorods and blocks finally assumed cylindrical shapes, as observed in the images as white spots. When the $KMnO_4$ concentration was low, less MnO_2 was produced; the tiny amounts of MnO_2 nanorods were unable to disperse the organic polymer blocks, and the inorganic substances and organic polymers formed lumps. When the concentration of $KMnO_4$ was increased, the MnO_2 production rate increased. Crystals could rapidly nucleate and crystallize to form micron-sized rods of uniform size. A large number of microrods could also effectively disperse a small amount of organic matter into a small-bulk morphology. The main mechanism may be related to the molecular-directing template of the PSS dopant. Inorganic MnO_2 can be grown on the active sites of the organic material, and PSS can be regarded as a cation-exchange resin; the undoped $-SO_3^-$ will react with the metal ions such that MnO_2 will grow in the vicinity of sulfonic acid in situ, followed by nucleation growth and the final formation of microrods. As shown in Fig. 5b, the simultaneous formation of MnO_2 microrods will also occur on the organic polymer block. Thus, Fig. 4h shows the ends of MnO_2 microrods with a small amount of polymer adhesion.

The TGA curve of the PEDOT:PSS/MnO_2 hybrid composite under the reaction of $n(KMnO_4)$ to n(EDOT) = 4:6and hydrothermal temperature of 80 °C shows that the material began to lose weight at 187 °C and lost approximately 1% of its mass mainly because of the volatilization of adsorbed water (Fig. 5a). The first maximum thermal decomposition temperature was 273 °C; this decomposition was mainly due to the decomposition of the sulfonic acid groups of the styrene ring in PSS. PSS decomposition was completed at 351 °C, with a mass loss of approximately 6%. Another decomposition of the composite occurred in the temperature range between 351 and 605 °C with a corresponding weight loss of 5%. This mass loss was mainly due to fracture and volatilization of the polymer molecular chain. At 800 °C, the PEDOT:PSS/MnO_2 hybrids still retained approximately 88% of their mass, illustrating that the mass ratio between organic and inorganic oxides was 12:88. The mass of MnO_2 in the synthesized material accounts for the majority of the inorganic oxides. These TG results further demonstrate that a large number of the nanotubes observed by SEM have morphologies similar to that of MnO_2 [47].

The conductivity curves of materials prepared under different hydrothermal temperatures and oxidant dosages are presented in Fig. 6. The electronic conductivity of samples was measured using four-probe conductivity meters, and the measured values were subsequently converted into electrical

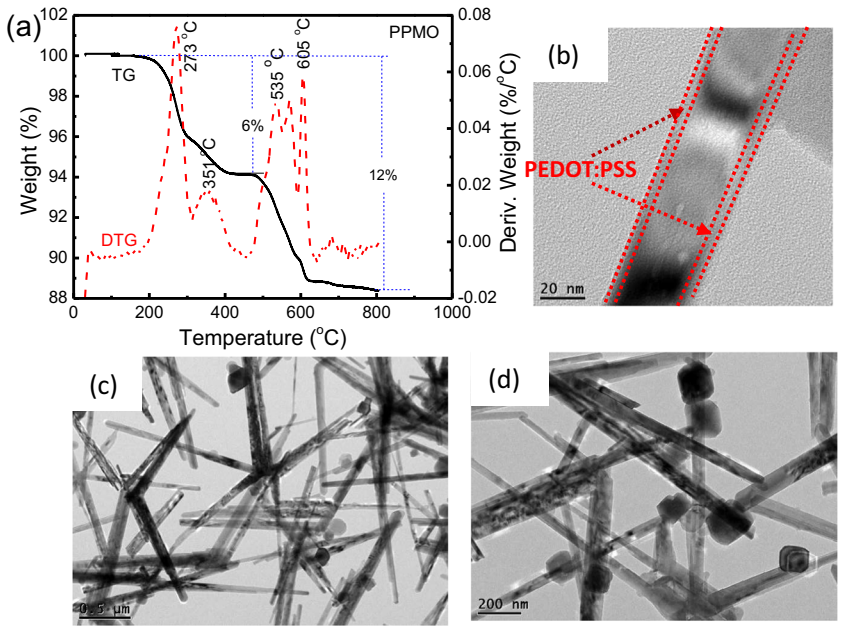

Fig. 5 Thermogravimetric curve and TEM images of preparation of samples under the optimal condition

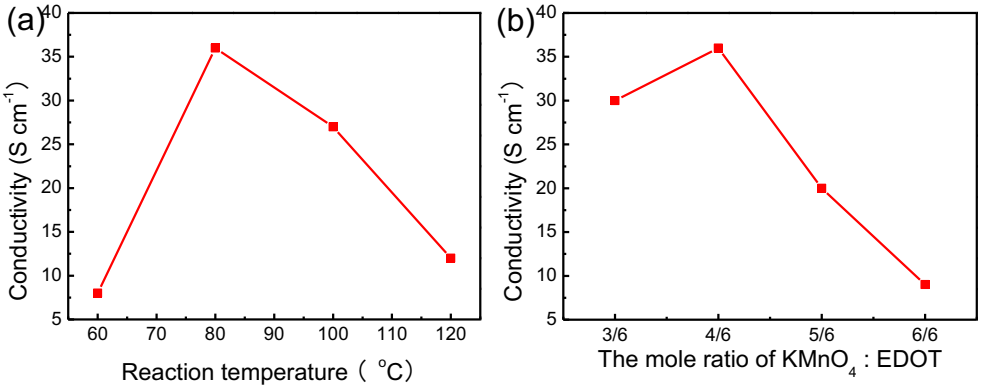

Fig. 6 Conductivity of materials prepared under different temperature and the ratio of oxidant

conductivity. Figure 6a shows that the conductivity of the composites increased to a maximum of 36 S cm^{-1} and then decreased with increasing temperature. This behavior is mainly attributed to the effect of temperature on the morphology of the material and to the stability of the organic skeleton; the polymer skeleton will collapse when the temperature is too high, resulting in carrier-hopping discontinuity and, thus, decreased conductivity. As shown in Fig. 6b, the conductivity of the material also presented a regular pattern of first increasing and then decreasing with increasing ratio of $KMnO_4$. First, the amount of $KMnO_4$ affected the oxidation degree of the polymer and the amount of inorganic MnO_2 formed. When the $KMnO_4$ concentration was lower, EDOT was not completely oxidized to form PEDOT, conductive network was not fully formed, PEDOT was over-oxidized and became rigid, and amount of inorganic MnO_2 was increased; consequently, the conductivity first increased and then decreased.

Electrochemical properties

The cyclic voltammograms of the PEDOT:PSS/MnO_2 hybrids prepared under different temperatures and different oxidant ratios of oxidant are shown in Fig. 7. The curves were collected using a three-electrode system, with a platinum electrode as the counter electrode, Ag/AgCl as the reference electrode, and active material as the working electrode; the scans were conducted at different scan rates from 10 to 200 mV s^{-1} with the electrodes immersed in 6 M KOH electrolyte. In the PEDOT:PSS/MnO_2 binary organic–inorganic hybrids, the main processes are the ion doping/doping process in the PEDOT skeleton ($[PEDOT^+]SO_3^- + e^- \rightleftharpoons [PEDOT_0] + SO_3^-$) and redox reactions between Mn^{4+} and Mn^{3+} ions via electron exchange in MnO_2 ($MnO_2 + yK^+ + e^- \rightleftharpoons yMnOOK + (1-y)MnO_2$). Cyclic voltammograms collected at different temperatures show that the redox reversibility of the materials

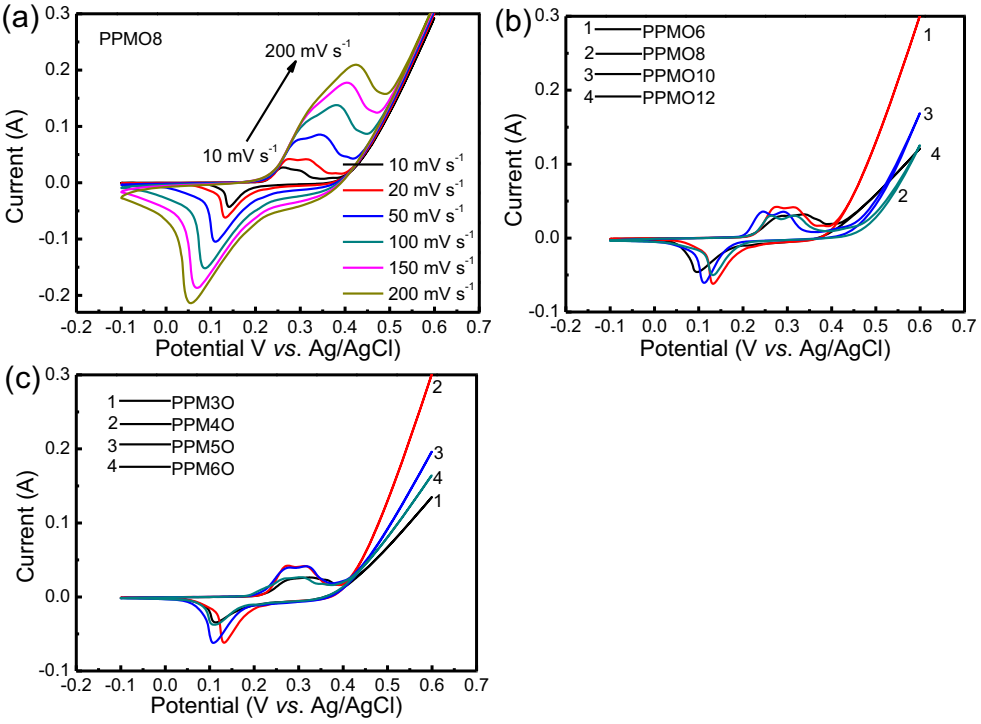

Fig. 7 Cyclic voltammetry curves of materials prepared under different temperature and the ratio of oxidant

prepared at different temperatures is better. In Fig. 7b, the area of the CV curve of the material prepared at 80 °C is the largest, indicating that the material has a high area-specific capacity at this temperature. As shown in Fig. 7c, the area of the CV curve reaches a maximum when the $KMnO_4$-to-EDOT molar ratio is 4:6, and the redox current reaches a maximum when the potential difference between the redox peaks is minimal. These results show that the 4:6 ratio is the best ratio for preparing the hybrid materials; it results in excellent electrode materials with minimum resistance and multiple electrochemically active sites [48].

To further explore the effect of the hydrothermal reaction temperature and oxidant molar ratio on the electrochemical properties of materials, galvanostatic charge, and discharge tests were performed with different materials under different current densities in 6 M KOH. The specific capacitance of materials prepared at different temperatures was calculated from Fig. 8a according to the discharge time; the specific capacities of the PPMO6, PPMO8, PPMO10, and PPMO12 were 223.6, 365.5, 332.7, and 236.4 F g^{-1} at a current density of 1 A g^{-1}, respectively. As evident from Fig. 8c, the rate capability of the four electrode materials was 65.1%, 89.5%, 76.5%, and 76.9%. The specific capacitance retentions of the materials were approximately 68%, 80%, 73%, and 58% after 2000 cycles. The PEDOT:PSS/MnO_2 prepared at a hydrothermal reaction temperature of 80 °C exhibited the best performance among the investigated samples, resulting in an electrode material with superior electrochemical performance. Low hydrothermal temperatures were not conducive for the formation of ordered crystals of MnO_2, which makes the recombination of inorganic matter easy; the interaction between organic matter and inorganic matter is weakened, which is not conducive for the formation of fast ions and electron channels. At the highest reaction temperature, MnO_2 exhibited reduced oxidation activity but accelerated thermal decomposition, resulting in multiphase MnO_2. Second, the oxidation of organic monomers is incomplete; thus, the organic-fiber-oriented template and material skeleton cannot be formed, precluding the formation of an

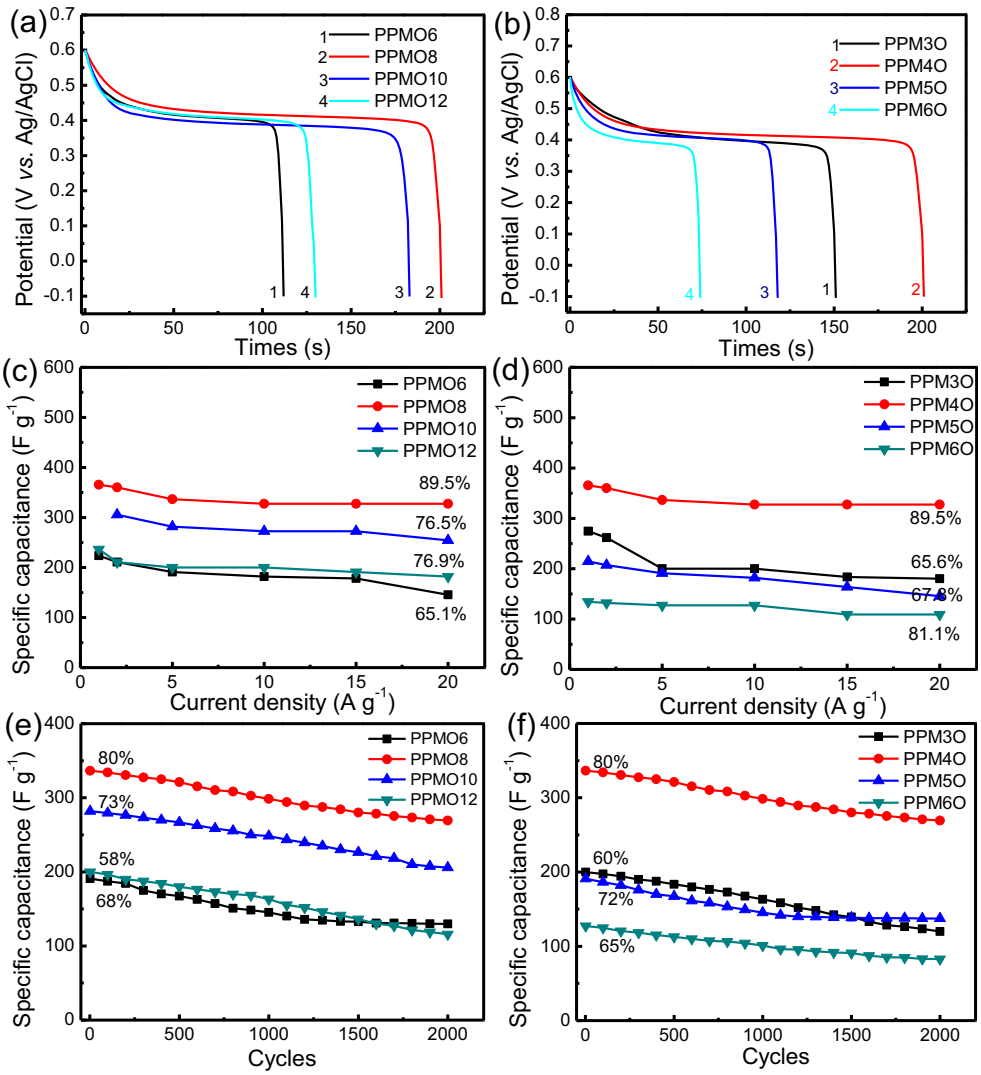

Fig. 8 **a** Galvanostatic discharge curves of PPMO6, PPMO8, PPMO10, and PPMO12 at 1 A g^{-1}. **b** Galvanostatic discharge curves of PPM3O, PPM4O, PPM5O, and PM6O at 1 A g^{-1}. **c** Specific capacitances of PPMO6, PPMO8, PPMO10, and PMO12 derived from the discharge curves at different current densities of 1, 2, 5, 10, 15, and 20 A g^{-1}. **d** Rate performance of PPM3O, PPM4O, PPM5O, and PPM6O. **e** Capacitance cycling performances of PPMO6, PPMO8, PPMO10, and PPMO12 at a current density of 5 A g^{-1}. (**f**) Capacitance cycling performances of PPM3O, PPM4O, PPM5O, and PPM6O at a current density of 5 A g^{-1}

Table 1 Comparison of Supercapacitor performance of composites based on PEDOT@MnO_2

Ref.	Composite	Electrolyte	Specific capacitor (F g^{-1})	Rate performance (%)	Stability(%)
[36]	Gro/PEDOT/MnO_2	0.5 M Na_2SO_4	195.7 at 0.5 A g^{-1}	26.0(0.5–10)	81.1 after 2000 cycles
[48]	α-MnO_2@δ-MnO_2	6 M KOH	310.2 at 20 A g^{-1}	49.6(1–20)	98.1 after 10,000 cycles
[50]	CNT:PEDOT/MnO_2	0.5 M Na_2SO_4	375 at 0.5 A g^{-1}	67.9	87.2 after 2000 cycles
[51]	MnO_2/PEDOT	1 M H_2SO_4	321.4 at 0.5 A g^{-1}	54(1–7)	90 after 4000 cycles
[52]	PEDOT/MnO_2	0.5 M Na_2SO_4	285 at 1 A g^{-1}	50(1–10)	99 after 1000 cycles
[53]	$ZnCo_2O_4$/MnO_2	1 M KOH	1526 at 10 A g^{-1}	65.2(1–10)	94.5 after 8000 cycles
[54]	$CoMoO_4$@MnO_2	1 M KOH	1037 at 0.04 A cm^{-2}	43.4	93 after 3000 cycles
[55]	$NiCo_2O_4$@MnO_2	1 M NaOH	906.7 at 0.04 A cm^{-2}	56.8	92.6 after 2000 cycles
[56]	MnO_2 nanorods	1 M Na_2SO_4	796 at 2 mV s^{-1}	25.2	95.5 after 3000 cycles
[57]	MnO_2	0.1 M KOH	750 at 1 mV s^{-1}	74.6(1–10)	183 after 3000 cycles
This work	PEDOT:PSS/MnO_2	6 M KOH	365.5 at 1 A g^{-1}	89.5(1–20)	80 after 2000 cycles

ordered nanotubular organic–inorganic composite of uniform size. Third, the stability of organic matter will be reduced in the higher-temperature environment, resulting in some degradation of the organic skeleton; the results of this reduced stability should be evident from the infrared spectra [49].

The electrochemical properties of materials prepared under different $KMnO_4$ molar ratios are shown in Fig. 8b, d, f. As shown in Fig. 8b, the specific capacities of PPM3O, PPM4O, PPM5O, and PPM6O were 274.5, 365.5, 214.5, and 134.5 F g^{-1}, respectively. The rate performances of the materials were 65.6%, 89.5%, 67.8%, and 81.1% at current densities ranging from 1 to 20 A g^{-1}. Compared with previously reported PEDOT:PSS/MnO_2 electrodes, those prepared in this work have a higher specific capacity and superior rate performance (see Table 1). The specific capacity retention rates of PPM3O, PPM4O, PPM5O, and PPM6O were 60%, 80%, 72%, and 65% after 2000 cycles at 5 A g^{-1}, respectively. The experimental results show that the $KMnO_4$-to-EDOT ratio strongly influenced the specific capacitance of the material. This influence likely stems from the role of $KMnO_4$ in the reaction. In the reaction, $KMnO_4$ plays the following roles. First, it oxidatively polymerizes the organic monomers. Second, during the process of oxidation, $KMnO_4$ releases OH^-, which regulates the pH of the reaction liquid; because the oxidation of $KMnO_4$ is affected by pH, it also affects the rate of reaction.

Conclusions

In summary, we reported a facile one-stop method to fabricate PEDOT:PSS/MnO_2 hybrids via a solvothermal method coupled with an oxidative polymerization process. With this combination, we obtained supercapacitor electrode materials with superior electrochemical performance. The PEDOT:PSS/MnO_2 hybrid material exhibits excellent capacitive properties: the specific capacitance can be as high as 365.5 F g^{-1} at 1 A g^{-1}, and the composite exhibits 80% retention of the specific capacitance after 2000 cycles at a high current density of 5 A g^{-1}. In particular, the composite exhibits a high-rate performance with 89.5% retention of the specific capacitance at current densities ranging from 1 to 20 A g^{-1}, and this is superior to the rate properties of previously reported single electrodes for supercapacitors. Meanwhile, the mechanism of formation of the composite nanorods was also revealed in the present work. Therefore, we believe that this method can be used to prepare advanced nanocomposite materials for use in supercapacitors and in devices for various applications.

Funding information This work was financially supported by Hunan Science and Technology Project, Grant No. 2013GK3002, and Science and Technology Project of Changsha (No. K1202039-11).

References

1. Chen S, Mani V, Saraswathi R (2014) Recent advancements in electrode materials for the high-performance electrochemical supercapacitors: a review. Int J Electrochem Sci 9:4072–4805
2. Zhang C, Deng YD, Hu WB, Qiao JL, Zhang L, Zhang J (2015) A review of electrolyte materials and compositions for electrochemical supercapacitors. Chem Soc Rev 44:7484–7539
3. Jabeen N, Hussain A, Xia Q, Sun S, Zhu J, Xia H (2017) High-performance 2.6 V aqueous asymmetric supercapacitors based on in situ formed $Na_{0.5}MnO_2$ nanosheet assembled nanowall arrays. Adv Mater 29:1700804
4. Jabeen N, Xia Q, Savilov SV, Aldoshin SM, Yu Y, Xia H (2016) Enhanced pseudocapacitive performance of α-MnO_2 by cation preinsertion. ACS Appl Mater Interfaces 8:33732–33740
5. Huang L, Chen DC, Ding YD, Feng S, Wang ZL, Liu ML (2013) Nickel–cobalt hydroxide nanosheets coated on $NiCo_2O_4$ nanowires grown on carbon fiber paper for high-performance pseudocapacitors. Nano Lett 13:3135–3139
6. Gumby J, Taberna PL, Simon P, Chesneau JFM (2001) Studies and characterisations of various activated carbons used for carbon/carbon supercapacitors. J Power Sources 101:109–116
7. Yang J, Yu C, Fan X, Liang S, Li S, Huang H, Ling Z, Hao C, Qiu J (2016) Electroactive edge site-enriched nickel–cobalt sulfide into

graphene frameworks for high-performance asymmetric supercapacitors. Energy Environ Sci 9:1299–1307
8. He XJ, Li XH, Ma H, Han JH, Zhang H, Yu C, Xiao N, Qiu JS (2017) ZnO template strategy for the synthesis of 3D interconnected graphene nanocapsules from coal tar pitch as supercapacitor electrode materials. J Power Sources 340:183–191
9. Xia H, Hong C, Shi X, Li B, Yuan G, Yao Q, Xie J (2015) Hierarchical heterostructures of Ag nanoparticles decorated MnO_2 nanowires as promising electrodes for supercapacitors. J Mater Chem A 3:1216–1221
10. Duay J, Sherrill SA, Gui Z, Gillette E, Lee SB (2013) Self-limiting electrodeposition of hierarchical MnO_2 and $M(OH)_2/MnO_2$ nanofibril/nanowires: mechanism and supercapacitor properties. ACS Nano 7:1200–1214
11. Du X, Wang CY, Chen MM, Jiao Y, Wang J (2009) Electrochemical performances of nanoparticle Fe_3O_4/activated carbon supercapacitor using KOH electrolyte solution. J Phys Chem C 113:2643–2646
12. Xia XH, Tu JP, Mai YJ, Wang XL, Gu GD, Zhao XB (2011) Self-supported hydrothermal synthesized hollow Co_3O_4 nanowire arrays with high supercapacitor capacitance. J Mater Chem 21:9319–9325
13. Yuan CZ, Zhang XG, Su LH, Gao B, Shen LF (2009) Facile synthesis and self-assembly of hierarchical porous NiO nano/micro spherical superstructures for high performance supercapacitors. J Mater Chem 19:5772–5777
14. Zhang GQ, Lou XW (2013) General solution growth of mesoporous $NiCo_2O_4$ nanosheets on various conductive substrates as high-performance electrodes for supercapacitors. Adv Mater 25:976–979
15. Jurewicz K, Delpeux S, Bertagna V, Béguin F, Frackowiak E (2001) Supercapacitors from nanotubes/polypyrrole composites. Chem Phys Lett 347:36–40
16. Ryu KS, Kim KM, Park NG, Park YJ, Chang SH (2002) Symmetric redox supercapacitor with conducting polyaniline electrodes. J Power Sources 103:305–309
17. Laforgue A (2011) All-textile flexible supercapacitors using electrospun poly (3, 4-ethylenedioxythiophene) nanofibers. J Power Sources 196:559–564
18. Kumar A, Welsh DM, Morvant MC, Piroux P, Abboud KA, Reynolds JR (1998) Conducting poly (3,4-alkylenedioxythiophene) derivatives as fast electrochromics with high-contrast ratios. Chem Mater 10:896–902
19. Liu DY, Reynolds JR (2010) Dioxythiophene-based polymer electrodes for supercapacitor modules. ACS Appl Mater Interfaces 2: 3586–3593
20. Zhao LP, Yang CM, Shen P, Wang ZY, Deng CF, Yang LS, Li JH, Qian D (2017) A brand-new strategy for remarkable improvements of electrochemical performances on conducting polymer-based flexible supercapacitors by coating Mo-Ni-P. Electrochim Acta 249:318–327
21. Wang HG, Lu ZG, Qian D, Li YJ, Zhang W (2007) Single-crystal α-MnO_2 nanorods: synthesis and electrochemical properties. Nanotechnology 18:115616
22. Chen S, Zhu JW, Wu XD, Han QF, Wang X (2010) Graphene oxide –MnO_2 nanocomposites for supercapacitors. ACS Nano 4:2822–2830
23. Bélanger D, Brousse L, Long JW (2008) Manganese oxides: battery materials make the leap to electrochemical capacitors. Electrochem Soc Interface 17:49
24. Kim JH, Lee KH, Overzet LJ, Lee GS (2011) Synthesis and electrochemical properties of spin-capable carbon nanotube sheet/MnO_x composites for high-performance energy storage devices. Nano Lett 11:2611–2617
25. Zhang H, Cao G, Wang Z, Yang Y, Shi Z, Gu Z (2008) Growth of manganese oxide nanoflowers on vertically-aligned carbon nanotube arrays for high-rate electrochemical capacitive energy storage. Nano Lett 8:2664–2668
26. Reddy ALM, Shaijumon MM, Gowda SR, Ajayan PM (2009) Coaxial MnO_2/carbon nanotube array electrodes for high-performance lithium batteries. Nano Lett 9:1002–1006
27. Peng L, Peng X, Liu B, Wu C, Xie Y, Yu G (2013) Ltrathin two-dimensional MnO_2/graphene hybrid nanostructures for high-performance, flexible planar supercapacitors. Nano Lett 13:2151–2157
28. Fan Z, Yan J, Wei T, Zhi L, Ning G, Li T, Wei F (2011) Asymmetric supercapacitors based on graphene/MnO_2 and activated carbon nanofiber electrodes with high power and energy density. Adv Funct Mater 21:2366–2375
29. He Y, Chen W, Li X, Zhang Z, Fu J, Zhao C, Xie E (2012) Freestanding three-dimensional graphene/MnO_2 composite networks as ultralight and flexible supercapacitor electrodes. ACS Nano 7:174–182
30. Liu J, Jiang J, Cheng C, Li H, Zhang J, Gong H, Fan HJ (2011) Co_3O_4 nanowire@MnO_2 ultrathin nanosheet core/shell arrays: a new class of high-performance pseudocapacitive materials. Adv Mater 23:2076–2081
31. Yan J, Khoo E, Sumboja A, Lee PS (2010) Facile coating of manganese oxide on tin oxide nanowires with high-performance capacitive behavior. ACS Nano 4:4247–4255
32. Yu Z, Thomas J (2014) Energy storing electrical cables: integrating energy storage and electrical conduction. Adv Mater 26:4297–4285
33. Kim YH, Sachse C, Machala ML, May C, Meskamp LM, Leo K (2011) Highly conductive PEDOT:PSS electrode with optimized solvent and thermal post-treatment for ITO-free organic solar cells. Adv Funct Mater 21:1076–1081
34. Groenendaal L, Jonas F, Freitag D, Pielartzik H, Reynolds JE (2000) Poly(3,4-ethylenedioxythiophene) and its derivatives: past, present, and future. Adv Mater 12:481–494
35. Liu R, Cho SI, Lee SB (2008) Poly(3,4-ethylenedioxythiophene) nanotubes as electrode materials for a high-powered supercapacitor. Nanotechnology 19:215710
36. Tang P, Han L, Zhang L (2014) Facile synthesis of graphite/PEDOT/MnO_2 composites on commercial supercapacitor separator membranes as flexible and high-performance supercapacitor electrodes. ACS Appl Mater Interfaces 6:10506–10515
37. Su ZJ, Yang C, Xu CJ, Wu HY, Zhang ZX, Liu T, Zhang C, Yang QH, Li BH, Kang FYK (2013) Co-electro-deposition of the MnO_2–PEDOT: PSS nanostructured composite for high areal mass, flexible asymmetric supercapacitor devices. J Mater Chem A 1:12432–12440
38. Yu ZN, Li C, Abbitt D, Thomas J (2014) Flexible, sandwich-like Ag-nanowire/PEDOT: PSS-nanopillar/MnO_2 high performance supercapacitors. J Mater Chem A 2:10923–10929
39. Liu R, Lee SB (2008) MnO_2/poly (3,4-ethylenedioxythiophene) coaxial nanowires by one-step coelectrodeposition for electrochemical energy storage. J Am Chem Soc 130:2942–2943
40. Duay J, Gillette E, Liu R, Lee SB (2012) Highly flexible pseudocapacitor based on freestanding heterogeneous MnO_2/conductive polymer nanowire arrays. Phys Chem Chem Phys 14: 3329–3337
41. Liu R, Duay J, Lee SB (2011) Electrochemical formation mechanism for the controlled synthesis of heterogeneous MnO_2/poly(3,4-ethylenedioxythiophene) nanowires. ACS Nano 5:5608–5619
42. Liu R, Duay J, Lee SB (2010) Redox exchange induced MnO_2 nanoparticle enrichment in poly(3,4-ethylenedioxythiophene) nanowires for electrochemical energy storage. ACS Nano 4: 4299–4307
43. Mai LQ, Dong F, Xu X, Luo YZ, An QY, Zhao YL, Pan J, Yang JN (2013) Cucumber-like V_2O_5/poly(3,4-ethylenedioxythiophene) & MnO_2 nanowires with enhanced electrochemical cyclability. Nano Lett 13:740–745
44. Zhang L, Peng H, Kilmartin PA, Soeller C, Travas-Sejdic J (2008) Poly(3,4-ethylenedioxythiophene) and polyaniline bilayer

nanostructures with high conductivity and electrocatalytic activity. Macromolecules 41:7671–7678
45. Wang J, Xu YL, Chen X, Du XF (2007) Electrochemical supercapacitor electrode material based on poly (3, 4-ethylenedioxythiophene)/polypyrrole composite. J Power Sources 163:1120–1125
46. Yin CJ, Yang CM, Jiang M, Deng CF, Yang LS, Li JH, Qian D (2016) A novel and facile one-pot solvothermal synthesis of PEDOT−PSS/Ni−Mn−Co−O hybrid as an advanced supercapacitor electrode material. ACS Appl Mater Interfaces 8:2741–2752
47. Zhou J, Ventura IA, Lubineau G (2014) Probing the role of PEDOT: PSS coated (MWCNTs) in thermal and mechanical properties of polycarbonate nanocomposites. Ind Eng Chem Res 53:3539–3549
48. Ma ZP, Shao GJ, Fan YQ, Wang GL, Shen DJ (2016) Construction of hierarchical α-MnO_2 nanowires@ultrathin δ-MnO_2 nanosheets core–shell nanostructure with excellent cycling stability for high-power asymmetric supercapacitor electrodes. ACS Appl Mater Interfaces 8:9050–9058
49. Cui LH, Cui J, Zheng HM, Wang Y, Wu YC (2017) Construction of $NiO/MnO_2/CeO_2$ hybrid nanoflake arrays as platform for electrochemical energy storage. J Power Sources 361:310–317
50. Sharma PK, Zhai L (2009) multiwall carbon nanotube supported poly(3,4-ethylenedioxythiophene)/manganese oxide nanocomposite electrode for super-capacitors. Electrochim Acta 54: 7148–7155
51. Yang YJ, Yuan WT, Li SB, Yang XJ, Xu JH, Jiang YD (2015) Manganese dioxide nanoparticle enrichment in porous conducting polymer as high performance supercapacitor electrode materials. Electrochim Acta 165:323–329
52. Tang PY, Zhao YQ, Xu CL (2013) Step-by-step assembled poly (3, 4-ethylenedioxythiophene)/manganese dioxide composite electrodes: tuning the structure for high electrochemical performance. Electrochim Acta 89:300–309
53. Qiu K, Lu Y, Zhang D, Cheng J, Yan H, Xu J, Liu X, Kim JK, Luo Y (2015) Mesoporous, hierarchical core/shell structured $ZnCo_2O_4$/MnO_2 nanocone forests for high-performance supercapacitors. Nano Energy 11:687–696
54. Zhang Z, Bao F, Zhang Y, Feng L, Ji Y, Zhang H, Sun Q, Feng S, Zhao X, Liu X (2015) Formation of hierarchical $CoMoO_4$@MnO_2 core–shell nanosheet arrays on nickel foam with markedly enhanced pseudocapacitive properties. J Power Sources 296:162–168
55. Bao F, Zhang Z, Guo W, Liu X (2015) Facile synthesis of three dimensional $NiCo_2O_4$@MnO_2 core–shell nanosheet arrays and its supercapacitive performance. Electrochim Acta 157:31–40
56. Kumar A, Sanger A, Kumar A, Mishra YK, Chandra R (2016) Performance of high energy density symmetric supercapacitor based on sputtered MnO_2 nanorods. ChemistrySelect 1:3885–3891
57. Ranjusha R, Nair AS, Ramakrishna S, Anjali P, Sujith K, Subramanian KRV, Balakrishnan A (2012) J Mater Chem 38:20465